

Negative differential resistance, perfect spin filtering effect and tunnel magnetoresistance in vanadium-doped zigzag blue phosphorus nanoribbons

Si-Cong Zhu^{*a,b}, Shun-Jin Peng,^a Kai-Ming Wu,^a Cho-Tung Yip,^d Kai-Lun Yao^c and Chi-Hang Lam^{*b}

^a College of Science and Key Laboratory for Ferrous Metallurgy and Resources Utilization of Ministry of Education, Wuhan University of Science and Technology, Wuhan 430065, China *E-mail: sczhu@wust.edu.cn

^b Department of Applied Physics, Hong Kong Polytechnic University, Hung Hom, Hong Kong, China * E-mail: C.H.Lam@polyu.edu.hk

^c Wuhan National High Magnetic Field Center and School of Physics, Huazhong University of Science and Technology, Wuhan 430074, China

^d Department of Physics, Shenzhen Graduate School, Harbin Institute of Technology, Shenzhen 518055, China

We investigate the electronic and transport properties of vanadium-doped zigzag blue phosphorus nanoribbons by first-principles quantum transport calculations. We study the spin-dependent transport properties and obtain current-voltage curves showing obvious spin polarization and negative differential behaviors. These interesting transport behaviors can be explained by the band structure of the vanadium-doped zigzag blue phosphorus nanoribbons. The tunnel magnetoresistance and spin filter effects under different magnetic configurations originates predominately from the symmetry matching between the band structures of the electrodes. According to our results, vanadium-doped zigzag blue phosphorus nanoribbons can be used as a perfect spin filter with a large tunnel magnetoresistance. This also indicates that blue phosphorus nanoribbons are a promising candidate for the future application in spintronics.

1. Introduction

Spintronics aims to utilize the spin degree freedom of electrons for novel information storage and logic devices.¹⁻³ Due to the potential applications in novel electronic devices, 2D materials, such as graphene, graphdyne, MoS₂ and silicene, are being study intensively in both theoretical and experimental researches in recent years.⁴⁻⁷ The ultra-low spin orbit coupling in graphene already made it to be one of the most promising candidates for spin

channel applications.⁸⁻¹⁴ The nanostructures of graphene such as nanoribbons, nanotubes, and their interconnections have opened up new directions for experimental and theoretical studies in the field of nanoelectronics.¹⁵ Black phosphorene (BP), a single layer of black phosphorus, had been successfully peeled off from bulk black phosphorus through mechanical exfoliation. BP has carrier mobility up to $1000 \text{ cm}^2/(\text{Vs})$, which is superior to other 2D semiconductors.¹⁶⁻¹⁸ Therefore, its outstanding electronic properties have aroused enormous interest for future electronic device applications.¹⁹⁻²⁴

As the allotrope of BP, blue phosphorus has a buckled honeycomb structure with a high stability. Unlike zero band gap graphene, blue phosphorus possesses a wider band gap (2.0 eV), which is remarkably higher than that of BP (0.5 eV).²⁵ Recently, Zhang and Xu had successfully grown monolayer blue phosphorous on Au (111) film via molecular beam epitaxy (MBE).^{26, 27}

Nanoribbons exhibit many exploitable electrical, optical, and magnetic properties.²⁸ In principle, black phosphorus can be etched or patterned along a specific lattice direction, forming nanoribbons for future nano-electronic devices.²⁹⁻³⁴ Furthermore, it has been a long-standing goal to achieve controllable magnetism in nonmagnetic 2D pristine materials, which can potentially facilitate the applications of these materials in recording media, magnetic inks, and spintronic devices.^{35, 36} However, unlike graphene and MoS_2 , blue phosphorene is not expected to show magnetism. A simple way to introduce magnetism in the blue phosphorene is by doping metals, which carry magnetic moments such as 3d transition-metal (TM) adatoms.³⁷ In this regard, it is of great significance to understand the electronic and magnetic behaviors of TM-decorated blue phosphorene (denoted as TM-BlueP systems hereafter) nanoribbons. Given that the reliable control of magnetic states is essential to the application of magnetic nanostructures, it is also indispensable to develop an effective method to control the magnetism of the TM-BlueP nanoribbon system. In our previous work, we investigate the electronic and magnetic properties of substitution metal atom impurities in two-dimensional (2D) blue phosphorene nanoribbons by using first-principles calculations. In impure zigzag blue phosphorene nanoribbons (zBPNRs), a metal atom is a substitute for P atom. The V-doped structure shows half-metallic properties.³⁸ So, we select V atom to dope zBPNR without any other element.

In this work, we study the spin current characteristics of doped zigzag blue phosphorene nanoribbons (zBPNR), with ab initio density functional theory calculation.^{39, 40} We demonstrate that V-substituted blue phosphorene nanoribbons possess magnetic properties. The transport properties are investigated through density functional theory combined with nonequilibrium Green's function (NEGF). In our calculations, relaxation of the whole system including atomic positions and spin-dependent electronic structures are all taken into account.

2. Computational methods

Optimization of all geometric structures are performed using the Atomistix ToolKit which is based on Density Functional Theory (DFT) as implemented in the well-tested SIESTA method combined with the NonEquilibrium Green's Function (NEGF) technique. The local density approximation (LDA) is utilized in the calculation with only valence electrons self-consistently calculated. An $8 \times 4 \times 2$ k mesh with the conjugate gradient algorithm is used. All the atomic positions are relaxed until the energy and the force on each atom are less than 10^{-5} eV and 0.05 eVÅ⁻¹, respectively.

After optimization, the subsequent spin-dependent transport properties of these systems are analyzed using by the density functional theory (DFT) and Keldysh nonequilibrium Green's function formalism (NEGF). In the transport calculations, the valence electronic orbitals are expanded in a double- ζ plus polarization (DZP) basis set for all atoms. The cutoff energy for the real space grid is set to 150 Ry and a $1 \times 1 \times 100$ k -points mesh is employed in the Brillouin zone for the electrodes. The spin-dependent transmission coefficients for the spin channels σ_{majority} and σ_{minority} at energy E and bias voltage V_b are calculated as:

$$T_{\sigma}(E, V_b) = \sum_{k_x, k_y} \text{Tr}[\text{Im} \Sigma_L^r G^r \text{Im} \Sigma_R^r G^a] \quad (1)$$

And

$$T_{\sigma}(E, V_b) = \text{Tr}[T_{\sigma}(E, V_b)] \quad (2)$$

where the trace is taken over the basis functions. Here G^r is a $2n \times 2n$ NEGF matrix where the factor 2 is due to the spin and n is the size of the basis set; Σ^r is the self-energy describing the coupling between the semi-infinite ferromagnetic leads and the scattering region which includes the pristine zBPNR segment and the two V-doped zBPNR leads. For our system, Σ_L^r is diagonal and given by

$$\sum_L^r(E) = \begin{pmatrix} \Sigma_{L_{\text{maj.}}}^r(E) & 0 \\ 0 & \Sigma_{L_{\text{min.}}}^r(E) \end{pmatrix} \quad (3)$$

For parallel configuration, Σ_R^r is similar to Σ_L^r . For parallel configuration is expressed as

$$\sum_R^r(E) = \begin{pmatrix} \Sigma_{R_{\text{maj.}}}^r(E) & 0 \\ 0 & \Sigma_{R_{\text{min.}}}^r(E) \end{pmatrix} \quad (4)$$

The spin-current (spin-polarized charge current) is calculated as:

$$J_{\sigma} = \int_{\mu_R}^{\mu_L} T_{\sigma}(E, V) [f(E - \mu_L) - f(E - \mu_R)] dE \quad (5)$$

where f is the Fermi-Dirac distribution, μ_L and μ_R are the chemical potentials of the left (L) and the right (R) leads.

3. Results and discussion

Fig. 1a shows a centre vanadium-doped 12-zBPNR (VE-zBPNR) model device. It consists of three parts: the left and right electrode contacts and the scattering region. In order to eliminate the dangling bonds, the edges of the nanoribbons are terminated by hydrogen atoms. Here, the left and right electrodes are modeled by a semi-infinite replica of the doped unit (see Fig. 1b) effectively expanding the modeled electrodes along the transport direction (i.e. x -direction) to $x = -\infty$ for the left electrode and $x = +\infty$ for the right electrode. We assume that the doping is performed by substituting a single phosphorus (P) atom close to the centre or the edge by a vanadium (V) atom every three zBPNR unit cells as shown in Fig. 1b. The right electrode is the same as the left one. The scattering region contains four pure unit cells, of which the leftmost cell belongs to the left electrode, and the rightmost cell belongs to the right electrode. They can screen the interaction between the electrodes and the center region, and serve as the buffering regions, as shown in Fig. 1a (The substrate is only displayed on the schematic to simulate experiment, actually, it is not been considered in our calculation). A vacuum layer, which is thicker than 15\AA , is used to eliminate interactions between periodic images in the Y and Z directions.

We substitute the V atom for the P atom at either the center or the edge position. To qualitatively verify the feasibility of our approach, we calculate the spin-resolved band structures of the electrode units (Fig. 1b), and the band structures are shown in Fig. 1c and 1d. Fig. 1c reveals that the V-center-doped zBPNR (VC-zBPNR) is half-metallic and that the spin-majority channel is metallic, while the spin minority channel is semiconducting. Our results also shows that, under the strong crystal field, the 3d orbitals of V split into $d_{x^2-y^2}$ (HOMO-1), d_{z^2} (HOMO) and d_{xy} (LUMO) orbitals (marked as (1)-(3)). The V-edge-doped (VE) lead unit cell exhibits the 3d orbitals $d_{x^2-y^2}$ (HOMO-1), d_{z^2} (HOMO) and d_{yz} (LUMO) (marked as 1-3) as shown in Fig. 1d. But because of the strong hybridization, the split energy level of d_{xy} (LUMO) orbitals for the V-centre-doped lead is higher than that for d_{xz} . This causes d_{xy} orbital to intersect the Fermi level (in the XY plane).

Experimentally, the magnetization of the left and the right electrodes can be aligned in either parallel spin configurations (PC) or antiparallel spin configurations (APC), which can be controlled by a sufficiently strong magnetic field. Therefore, in our 2D systems, the PC and APC spin configurations can be used to study the spin-polarized transport properties. The inset of Fig. 2c shows the spin alignment of the centre VC-zBPNR system for the PC and APC spin configurations. Fig. 2a and 2b display the spin-resolved I-V curves of the VC-zBPNR and

VE-zBPNR systems for the PC and APC spin configurations.

From Fig. 2(a), the PC and APC majority-spin currents are nonlinear and in the off state for the bias voltage ranging from [0 V - 0.5 V]. When the positive bias is further increased, the currents of the majority-spin increase rapidly. The PC and APC minority-spin currents become off state when the bias is equal to 1.5V. To observe the variation of the current at low bias, we plot the I-V characteristics for spin configurations in semi-log scales, as illustrated in Fig. 2(a). The majority-spin currents are four orders of magnitude larger than that of the minority-spin currents at low bias. It also demonstrates nearly perfect spin filter effect (SFE) causing by the 100% spin polarizations at the bias voltage ranging from 0.1 to 1.5V as shown in Fig. 3(b). When the bias voltage is in between 1.5V and 1.8V, the majority-spin decreases rapidly, showing a significant negative differential effect (NDR-a property of some electrical circuits and devices in which an increase in voltage across the device's terminals results in a decrease in electric current through it.). In Fig. 2(b), the majority- and minority-spin currents of the VE-zBPNR system are less than the VC-zBPNR ones. Moreover, the PC and APC majority-spin currents are both nonlinear and in the off state for a bias voltage ranging from 0 V to 1.0 V. When the positive bias is increased, the currents of the majority-spin are turned on and increase rapidly. The PC and APC minority-spin currents cut off when the bias is 1.5V. To observe the variation of current at low bias, we also plot the I-V characteristics in semi-log scales in the set in Fig. 2(b). The majority-spin currents are larger than the minority-spin currents at low bias and demonstrates high spin filter effect (SFE) as shown in Fig. 3(d) [at bias 0.8-1.4V]. When the bias is from 1.6V to 1.8V, the majority-spin current similarly decreases rapidly, showing a significant negative differential effect (NDR) effect. Fig. 2(c) and (d) show the total PC and APC currents of the two systems. When the bias is higher than 1.0V, the PC and APC currents in time-current curves can cross each other. But at low bias, the two junctions possess a large tunneling magnetoresistance(TMR) ratio.

In Fig. 3(a) and (c), plots the TMR ratio defined as $R_{TMR} = |(I_{PC} - I_{APC})/I_{APC}| \times 100\%$, where I_{APC} and I_{PC} are the total currents for PC and APC at the same bias, respectively. TMR of around $10^6\%$ and $10^9\%$ are obtained at 0.1V bias as calculated from the equilibrium conductance. This behavior shows that the device at the V doped-zBPNR junctions can also be used as a spin valve.

To gain further insight into the transport mechanism in these structures, we calculate the spin-dependent transmission spectra as a function of electron energy E and bias voltage for the VC-zBPNR and VE-zBPNR junctions. The transmission spectra of the spin transport with spin alignment in the PC and APC setups are shown in Fig. 4(a) and 4(b) for the VC-zBPNR system. In a PC majority-spin state, the transport peaks enter the bias window for a bias if 1.1V (Region I), leading to a rapid increase of current as shown in Fig. 2(a). However, when the bias exceeds 1.5 V, the transmission peaks in the bias window are reduced (Region II). When the bias voltage is

higher than 1.8 V, the bias window again includes the transmission peaks, leading to another rapid increase of the current (Region III). In the PC minority-spin state setup, no transmission peak enters the bias window of [0V, 1.5 V], leading to the suppression of the minority current. When the bias is increased further, only a small portion of the transmission spectra moves into the bias window (Region I), and then the minority current increases by only a small amount (Region II). As a result, it is up to SFE 100% based on the PC setup of VC-zBPNR junction. In the APC junction, the transmission spectra show characteristics similar to those of the PC ones (Fig. 4b).

In Fig. 4(c) and (d), for the VE- zBPNR junction, the spin transmission spectra have certain features in common with the VC-zBPNR, but at variance in two respects. First, when the bias is applied, the shifts of transmission spectral peaks are less pronounced, and fewer transmission peaks move to energy bias windows. Second, the effective number of transmission channels in the bias window is slightly less than that for VC- zBPNR, and this leads to a slightly smaller spin current in Fig. 2(b).

Moreover, the transmission spectra describe electron transmission between the two electrodes. As previously discussed when the symmetry of the spin subbands of the electrodes matches, the transmission channel is open. When they differ, the channel is closed. Likewise, Fig. 5 shows that the I-V characteristics and transmission spectra. We take the conditions of three typical bias (0V (a), 1.5V(c), and 1.8V (e)) of the device VC- zBPNR and two magnetization configurations (PC and APC) for example. Fig. 5 displays the band structures of the left electrode (left panel) and the right electrode (right panel) along with the transport coefficient (middle panel) under in different conditions.

We label the majority-spin 3d bands of the left and the right electrodes near the Fermi level with the symbols $W1$, $W2$ and $W3$, and the minority bands of the right electrode in the vicinity of the Fermi level with the symbols $W1'$, $W2'$ and $W3'$, respectively. The shadow frame represents the efficacious transmission channel of majority-spin (minority-spin) electrons within the bias window, which has a detectable effect to the spin-depended transmission. In Fig. 5(a), for the PC majority-spin, the left subbands have the same symmetry with the right one, so the transport channel is opened. There is a transmission peak of the majority-spin channel near the Fermi level, while the minority-spin channel has no transmission band near or below the Fermi level. Thus a perfect spin filtering behavior is anticipated in the PC system.

When a bias is added to the electrodes, a positive (negative) bias moves the energy bands upward (downward). The movement of the bands leads to a variation of the symmetry matching between the left and the right leads. For both majority- and minority-spin electrons in Fig. 5, the W_n subbands on the left and the W_n' subbands on the right have mismatched symmetry and the transport channel will be closed. Here, the bands for two other typical biases (1.5 V and 1.8 V) are

shown in Fig. 5c and 5e, and the bias window is indicated by the shaded regions. As seen from Fig. 5c, because of the shifts of the band structures, the symmetry is changed within the bias window. The energy levels at the two electrodes are matched for a bias in [0.4-0.75eV]. For other biases, the left subbands and the right subbands have different symmetries, so the transport channel is closed. For the spin-down condition, the efficacious transport channel is below the Fermi level. However, because of the symmetry mismatching, the transport channel is still closed. When the bias voltage is further increased to 1.8V (Fig. 5e), the bias window enlarge. Though the symmetry is matching, the range of efficacious transmission channels in [0.6-0.9eV] is reduced. As a result, the majority-spin dependent current falls suddenly for bias 1.8V. Some other minority-spin subbands show the same symmetry as the right electrode, leading some transmission peaks channels, and the minority-spin current increase rapidly (Fig. 2a).

In contrast, for the APC (Fig. 5b, 5d and 5f), we take the conditions of three typical biases (0V (b), 1.6V (d), and 1.9V (f)) as examples. In a wide energy range, the majority-spin and minority-spin transmission peaks in the vicinity of the Fermi level are almost suppressed. These phenomena can be deduced from the band structures of the electrodes, as there are only majority-spin bands near the Fermi level ($W1, W2$ and $W3$) of left electrode and minority-spin bands near the Fermi level ($W1', W2'$ and $W3'$) of the right electrode.

In APC configuration, with a 0 V bias, since the spin orientation of left electrode is up and the right one is down, the spin-resolved band structures are changed and shown in the left and right panels of Fig. 5b. Around the Fermi level, for the majority-spin, the left subband (W_n) and the right subbands (W_n') have different symmetries, so both the majority- and minority-spin transport channels are closed. Therefore, a zero transmission spectra can be seen in the transport spectrum (Fig. 5b middle panel). When the bias voltage is added, the shifts of the left and the right band structures lead to two diametrically different consequences to majority-spin and minority-spin transport channels. When the bias reaches between 1.6 V and 1.9V (Fig. 5d, 5f), the transmission and band structures show a similar character as the PC system.

The above analysis indicates that the current of the majority-spin channel through the PC and APC systems are larger than that of minority-spin channel. The current-voltage curve displays obvious spin-filter behaviors, implying that the 2D material can be a promising building block for designing 2D spintronics devices. From Fig. 6a, one can see the molecular projected self-consistent Hamiltonian (MPSH) eigenvalues for VC-zBPRN device shift to the low energy area by increasing the forward bias from 0 V to 2.0 V. Figs 6b and 6c show the spin transmission spectra within the energy range from 0.4 to 1.0 eV at bias 1.5 and 1.8 V. Here, the Fermi level is set as zero for clarity, and the inverted triangles stand for the eigenvalues of the MPSH, which can be referred to as perturbed molecular orbitals (MOs). Apparently, for the majority-spin of

VC-zBPNR PC system with a bias reaching 1.5V, the majority-spin electron passing through the scattering region has several broad transmission peaks located within 4.0 and 1.0 eV (from LUMO+4 to LUMO+6). In contrast, for a bias voltage 1.8 V, the transmission peaks are less significant as the energy range of 0.4 and 1.0 eV and have much denser bands than at a bias 1.5V (from LUMO+5 to LUMO+8).

The conductive capability of the nanoribbon is determined not only by the energy of the molecular orbitals near the Fermi level but also by the spatial distribution of the frontier molecular orbital. Hence, to understand the origin of these transmission peaks around E_F and their changes upon the increase of the bias, we calculate the spatial distribution of the MPSH eigenvalues which have a contribution to current integral at 1.5 V and 1.8 V.

Table 1 shows the spatial contribution of these MPSH eigenstates, for 1.5V: LUMO+4, LUMO+5 and LUMO+6, for 1.8V: LUMO+5, LUMO+6, LUMO+7, LUMO+8, LUMO+9, LUMO+10, LUMO+11 and LUMO+12, which are all in the bias window. We can see that at bias voltage 1.5V, the three MPSH eigenstates are not localized along the X direction. When the bias voltage is increased to 1.8 V, the spatial contribution of LUMO+5 and LUMO+6 are reduced. In particular, the molecular orbital states of scattering region P atoms are most reduced. For the new channels, only LUMO+8 shows the nonlocal characteristic along the X direction. The other channels are all localized. The reduction and localization weaken the coupling between the scattering region and the left (right) electrode, and then the electrons entering the device from one electrode cannot leave the junction again and reach the end. As a result, the transmission through the nanoribbon junction will be suppressed and the current will be decreased. The majority-spin current of PC system thus shows significant negative differential resistance (NDR) effect.

4. Conclusion

In summary, we have carried out first-principles calculations in combination with the NEGF approach to examine the spin polarized transport of vanadium centre- and edge-doped zigzag blue phosphorus nanoribbons. Perfect spin filter efficiency with almost 100% spin polarization, TMR and NDR behaviors can be obtained by tuning the external magnetic field in vanadium centre- and edge-doped zBPNRs devices. But for edge-doped zBPNRs devices, the TMR can reach 10^9 . The spin filter behavior mainly originates from the shifts of the energy levels of Vanadium 3d electrons at the electrodes. The different conductive properties of zBPNRs in the PC and APC states lead to a giant magnetoresistance effect with a large magnetoresistance ratio. The above results indicate that this V doped zBPNRs can be applied in multifunctional 2D spintronic devices.

Acknowledgements

The authors would like to acknowledge the support from *Hong Kong Scholars Program No. XJ2016007*, National Natural Science Foundation of China under Grants No. 11704291, No.11647047, No. 11504078 and No. 11704292, and HK PolyU under Grant No. G-YBHY, and foundation for University Key Teachers from the WUST of No. 2017xz024.

Notes and references

1. S. Wolf, D. Awschalom, R. Buhrman, J. Daughton, S. Von Molnar, M. Roukes, A.Y. Chhtchelkanova, D. Treger, *Science* 2001, **294**, 1488.
2. I. Žutić, J. Fabian, S.D. Sarma, *Rev. Mod. Phys.* 2004, **76**, 323.
3. A. Fert, *Rev. Mod. Phys.* 2008, **80**, 1517.
4. B. Dlubak, M.-B. Martin, C. Deranlot, B. Servet, S. Xavier, R. Mattana, M. Sprinkle, C. Berger, W.A. De Heer, F. Petroff, *Nat. Phys.* 2012, **8**, 557.
5. M. Guimarães, P. Zomer, J. Ingla-Aynés, J. Brant, N. Tombros, B. Van Wees, *Phys. Rev. Lett.* 2014, **113**, 086602.
6. W. Han, R.K. Kawakami, M. Gmitra, J. Fabian, *Nat. Nanotechnol.* 2014, **9**, 794.
7. A.K. Geim, I.V. Grigorieva, *Nature* 2013, **499**, 419.
8. Y. Ni, X. Wang, W. Tao, S.-C. Zhu, K.-L. Yao, *Sci. Rep.* 2016, **6**, 25914.
9. P. Vogt, P. De Padova, C. Quaresima, J. Avila, E. Frantzeskakis, M.C. Asensio, A. Resta, B. Ealet, G. Le Lay, *Phys. Rev. Lett.* 2012, **108**, 155501.
10. E. Bianco, S. Butler, S. Jiang, O.D. Restrepo, W. Windl, J.E. Goldberger, *Acs Nano* 2013, **7**, 4414.
11. S. Bader, S. Parkin, *Annu. Rev. Condens. Matter Phys.* 2010, **1**, 71.
12. N. Tombros, C. Jozsa, M. Popinciuc, H.T. Jonkman, B.J. Van Wees, *Nature* 2007, **448**, 571.
13. W. Han, K. Pi, K. McCreary, Y. Li, J.J. Wong, A. Swartz, R. Kawakami, *Phys. Rev. Lett.* 2010, **105**, 167202.
14. W. Han, R.K. Kawakami, *Phys. Rev. Lett.* 2011, **107**, 047207.
15. S. Zhang, C. Li, S. Li, Q. Sun, Z. Guo, Y. Jia, *Appl. Phys. Lett.* 2014, **104**, 172111.
16. J. Qiao, X. Kong, Z.-X. Hu, F. Yang, W. Ji, *Nat. Commun.* 2014, **5**, 4475.
17. L. Li, Y. Yu, G.J. Ye, Q. Ge, X. Ou, H. Wu, D. Feng, X.H. Chen, Y. Zhang, *Nat. Nanotechnol.* 2014, **9**, 372.
18. C.H. Zhang, G. Xiang, M. Lan, Z.J. Tang, L.D. Deng, X. Zhang, *RSC Adv.* 2015, **5**, 40358.
19. Z. Zhu, C. Li, W. Yu, D. Chang, Q. Sun, Y. Jia, *Appl. Phys. Lett.* 2014, **105**, 113105.
20. V. Tran, R. Soklaski, Y. Liang, L. Yang, *Phys. Rev. B* 2014, **89**, 235319.
21. R. Fei, L. Yang, *Nano. Lett.* 2014, **14**, 2884.
22. R. Fei, L. Yang, *Appl. Phys. Lett.* 2014, **105**, 083120.
23. V. Tran, L. Yang, *Phys. Rev. B* 2014, **89**, 245407.
24. Z.-L. Zhu, W.-Y. Yu, X.-Y. Ren, Q. Sun, Y. Jia, *Europhys. Lett.* 2015, **109**, 47003.
25. Z. Zhu, D. Tománek, *Phys. Rev. Lett.* 2014, **112**, 176802.
26. J.L. Zhang, S. Zhao, C. Han, Z. Wang, S. Zhong, S. Sun, R. Guo, X. Zhou, C.D. Gu, K.D. Yuan, *Nano Lett.* 2016, **16**, 4903.
27. J.-P. Xu, J.-Q. Zhang, H. Tian, H. Xu, W. Ho, M. Xie, *Phys. Rev. Mater.* 2017, **1**, 061002.

28. H. Sevinçli, M. Topsakal, E. Durgun, S. Ciraci, *Phys. Rev. B* 2008, **77**, 195434.
29. Y. Cai, Q. Ke, G. Zhang, Y.-W. Zhang, *J. Phys. Chem. C* 2015, **119**, 3102.
30. V.V. Kulish, O.I. Malyi, C. Persson, P. Wu, *Phys. Chem. Chem. Phys.* 2015, **17**, 992.
31. D. Boukhvalov, A. Rudenko, D. Prishchenko, V. Mazurenko, M. Katsnelson, *Phys. Chem. Chem. Phys.* 2015, **17**, 5209.
32. G. Qin, Q.-B. Yan, Z. Qin, S.-Y. Yue, M. Hu, G. Su, *Phys. Chem. Chem. Phys.* 2015, **17**, 4854.
33. X. Liu, Y. Wen, Z. Chen, B. Shan, R. Chen, *Phys. Chem. Chem. Phys.* 2015, **17**, 16398.
34. H. Zheng, J. Zhang, B. Yang, X. Du, Y. Yan, *Phys. Chem. Chem. Phys.* 2015, **17**, 16341.
35. J. Li, G. Zhou, Y. Chen, B.-L. Gu, W. Duan, *J. Am. Chem. Soc.* 2009, **131**, 1796.
36. C. Gong, L. Li, Z. Li, H. Ji, A. Stern, Y. Xia, T. Cao, W. Bao, C. Wang, Y. Wang, *Nature* 2017, **546**, 265.
37. W. Yu, Z. Zhu, C.-Y. Niu, C. Li, J.-H. Cho, Y. Jia, *Nanoscale Res. Lett.* 2016, **11**, 77.
38. S.-C. Zhu, C.-T. Yip, S.-J. Peng, K.-M. Wu, K.-L. Yao, C.-L. Mak, C.-H. Lam, *Phys. Chem. Chem. Phys.* 2018, **20**, 7635.
39. P. Hohenberg, W. Kohn, *Phys. Rev.* 1964, **136**, B864.
40. W. Kohn, L.J. Sham, *Phys. Rev.* 1965, **140**, A1133.

Fig. 1

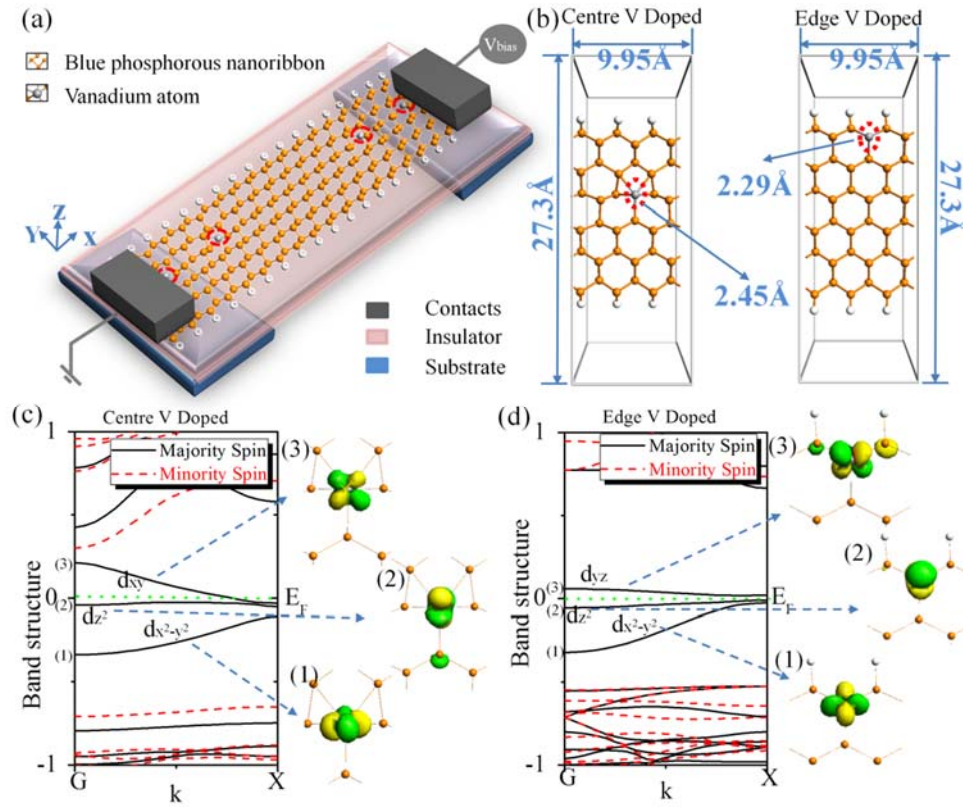


Fig. 1 (a) A schematic diagram of a model device with semi-infinite left leads and right leads. (b) The two-dimensional infinite 12-zBPNR with V centre-doped and V edge-doped, the average bond lengths of V atom and most nearest P atoms are showed between with the two bulks. Calculated band structure of V centre-doped (c) and V edge-doped (d) 12-zBPNR. The labels (1)–(3) of the band structure refer to crystalline orbitals of the wire calculated for the Γ point.

Fig. 2

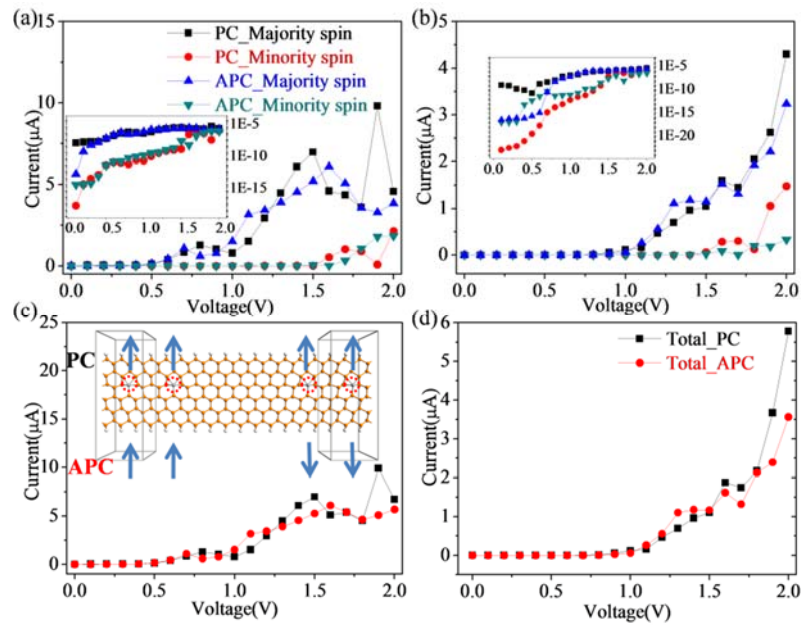


Fig. 2 Spin polarized I-V curves for PC and APC setups of the magnetizations at the leads for the (a)VC-zBPNR and (b)VE-zBPNR systems. (c)I-V curves for total current of PC and APC for the VC-zBPNR and (d)VE-zBPNR systems.

Fig. 3

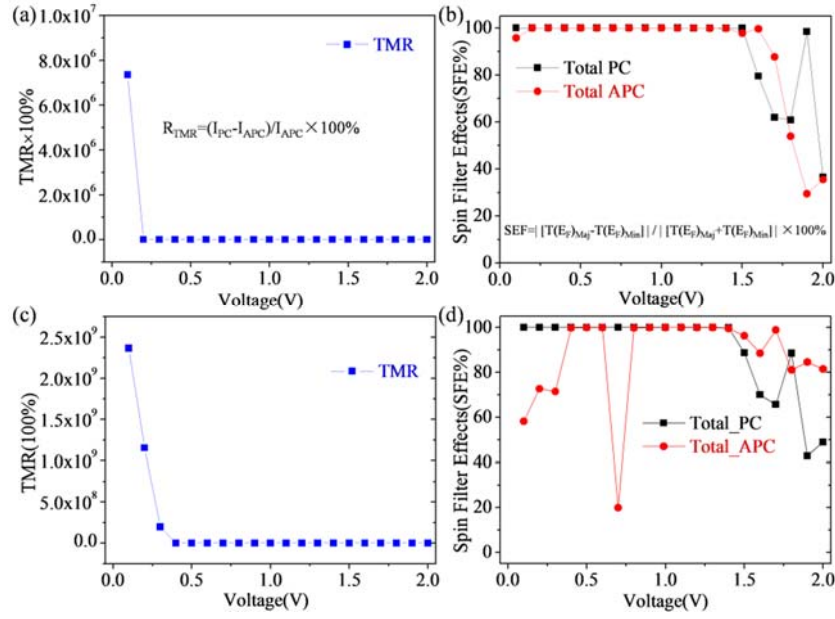


Fig. 3 TMR of the (a)VC-zBPNR and (c)VE-zBPNR systems as a function of bias. $R_{TMR} = (I_{PC} - I_{APC}) / I_{APC} \times 100\%$. Also shown is the SEF of (b)VC-zBPNR and (d)VE-zBPNR systems as a function of bias.

Fig. 4

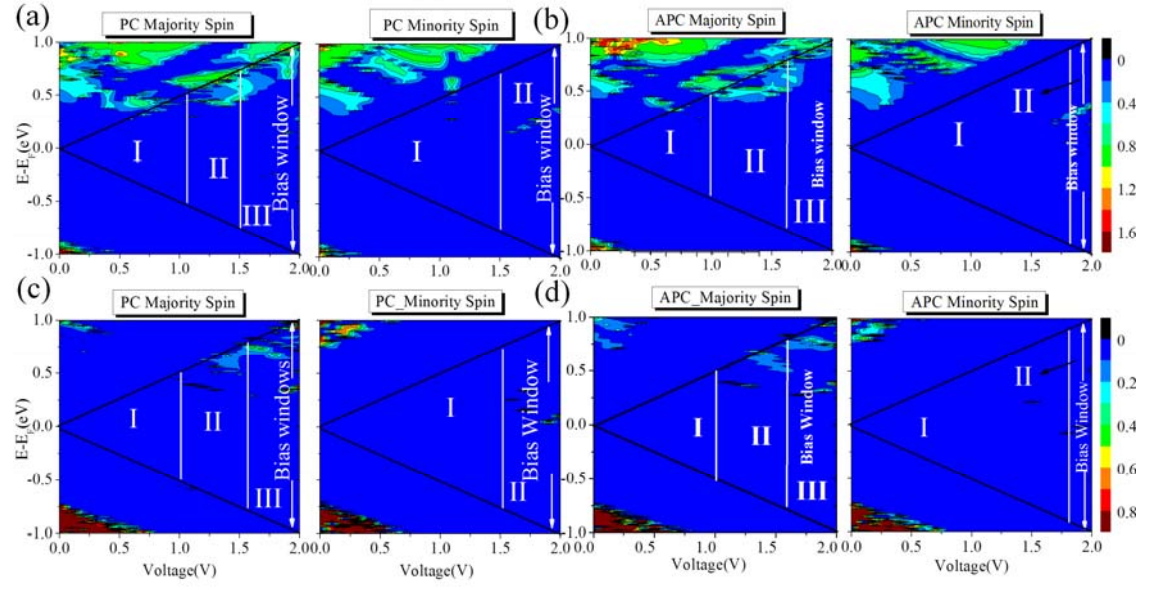


Fig. 4 Spin-dependent transmission spectra as a function of electron energy E and bias voltage for VC-zBPNR systems in (a) PC state and (b) APC states, and for VE-zBPNR systems in (c) PC and (d) APC states.

Fig. 5

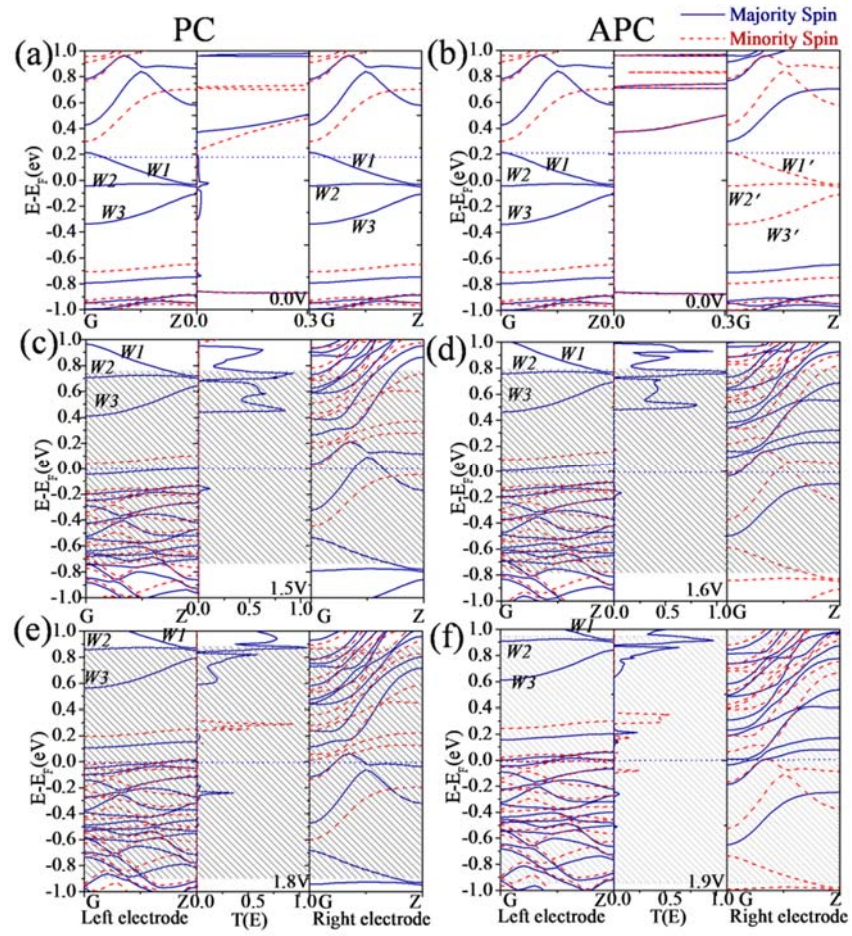


Fig. 5 The spin-resolved band structures and the transmission spectra. The spin-resolved band structures for the PC setup at biases of 0.0 V (a), 1.5 V (c), and 1.8 V and for the APC setup at biases of 0.0 V (b), 1.6 V (d) and 1.9 V (f) for the VE-zBPNR systems. The blue solid and red dotted curves correspond to the majority-spin and minority-spin channels, respectively. The Fermi level is at zero energy and is indicated by a blue dotted line.

Fig. 6

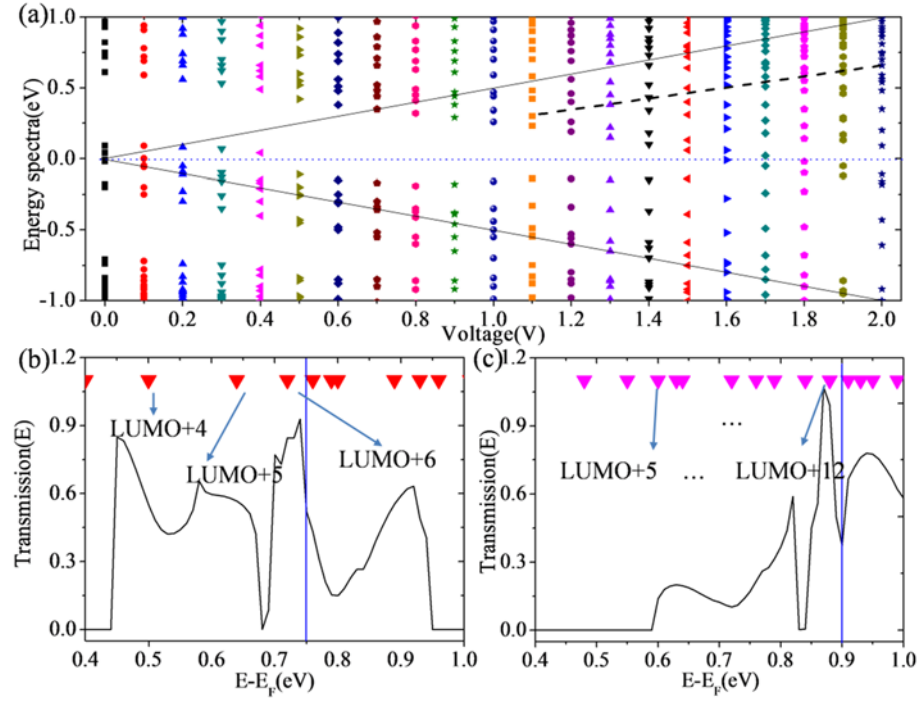
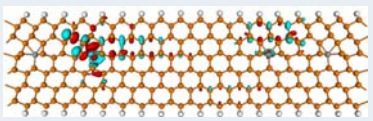
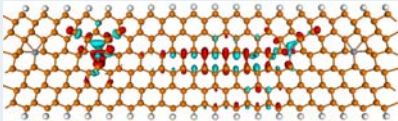
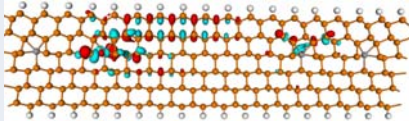
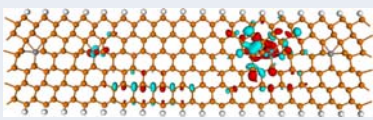
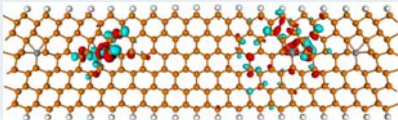
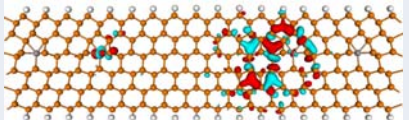
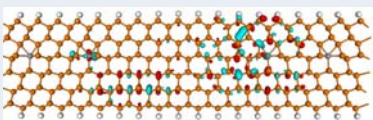
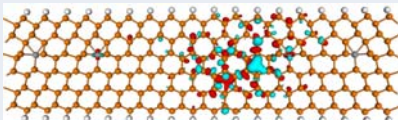
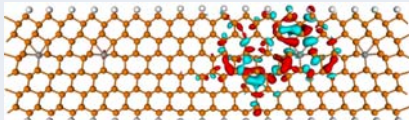


Fig. 6 (a) The energy spectrum depending on the bias for the VE-zBPNR systems. The range of bias voltage is from 0.0 V to 2.0 V. (b) Spin-resolved transmission spectra of VE-zBPNR systems at $V = 1.5$ V (b) and $V = 1.8$ V (c).

Table 1

Table 1 The spatial distribution of the MPSH eigenstates of VE-zBPNR systems at 1.5 V and 1.8 V.

voltage	MPSH(Angstrom ^{-3/2})	MPSH(Angstrom ^{-3/2})	MPSH(Angstrom ^{-3/2})
1.5V	LUMO+4	LUMO+5	LUMO+6
			
1.8V	LUMO+5	LUMO+6	LUMO+7
			
	LUMO+8	LUMO+9	LUMO+10
			
	LUMO+11	LUMO+12	
	